

THE DYNAMICS, APPEARANCE AND DEMOGRAPHICS OF RELATIVISTIC JETS TRIGGERED BY TIDAL DISRUPTION OF STARS IN QUIESCENT SUPERMASSIVE BLACK HOLES

FABIO DE COLLE, JAMES GUILLOCHON, JILL NAIMAN AND ENRICO RAMIREZ-RUIZ¹*Draft version March 3, 2013*

ABSTRACT

We examine the consequences of a model in which relativistic jets can be triggered in quiescent massive black holes when a geometrically thick and hot accretion disk forms as a result of the tidal disruption of a star. To estimate the power, thrust and lifetime of the jet, we use the mass accretion history onto the black hole as calculated by detailed hydrodynamic simulations of the tidal disruption of stars. We go on to determine the states of the interstellar medium in various types of quiescent galactic nuclei, and describe how this external matter can affect jets propagating through it. We use this information, together with a two-dimensional hydrodynamic model of the structure of the relativistic flow, to study the dynamics of the jet, the propagation of which is regulated by the density stratification of the environment and by its injection history. The breaking of symmetry involved in transitioning from one to two dimensions is crucial and leads to qualitatively new phenomena. At early times, as the jet power increases, the high pressure of the cocoon collimates the jet, increasing its shock velocity as compared to that of spherical models. We show that small velocity gradients, induced near or at the source, steepen into internal shocks and provide a source of free energy for particle acceleration and radiation along the jet's channel. The jets terminate at a working surface where they interact strongly with the surrounding medium through a combination of shock waves and instabilities; a continuous flow of relativistic fluid emanating from the nucleus supplies this region with mass, momentum and energy. Information about the $t^{-5/3}$ decrease in power supply propagates within the jet at the internal sound speed. As a result, the internal energy at the jet head continues to accumulate until long after the peak feeding rate is reached. An appreciable time delay is thus expected between peaks in the short-wavelength radiation emanating near the jet's origin and the long-wavelength emission produced at the head of the jet. Many of the observed properties of the Swift 1644+57/GRB 110328A event can be understood as resulting from accretion onto and jets driven by a $10^6 M_\odot$ central mass black hole following the disruption of sun-like star. With the inclusion of a stochastic contribution to the luminosity due to variations in the feeding rate driven by instabilities near the tidal radius, we find that our model can explain the X-ray light curve without invoking a rarely-occurring deep encounter. In conjunction with the number density of black holes in the local universe, we hypothesize that the conditions required to produce the Swift event are not anomalous, but are in fact representative of the jet-driven flare population arising from tidal disruptions.

Subject headings: accretion, accretion disks — gamma rays: bursts — hydrodynamics — methods: numerical — relativity — shock waves

1. INTRODUCTION

Relativistic jets accelerated from compact objects, such as neutron stars or black holes, are suspected to produce many of the observational signatures associated with high energy phenomena. Objects thought to produce them include radio galaxies and quasars (Begelman et al. 1984), microquasars (Mirabel & Rodríguez 1999) and gamma ray bursts (Gehrels et al. 2009). An important difference between jets of gamma ray bursts and the better studied radio jets of quasars or microquasars is that active quasars inject energy over extended periods of time into the jet while gamma ray burst sources are impulsive. Therefore, quasar jets remain highly collimated throughout their lifetimes, while gamma ray burst jets decelerate and expand significantly once they become non relativistic (Ayal & Piran 2001; Ramirez-Ruiz & MacFadyen 2010).

Recent observations of the Swift 1644+57/GRB 110328A event (Bloom et al. 2011; Burrows et al. 2011; Levan et al. 2011) and of the Swift J2058.4+0516 event (Cenko et al. 2011) have been interpreted (Bloom et al. 2011; Giannios & Metzger 2011; Metzger et al. 2012; Miller Gültekin 2011; Shao et al. 2011; Zauderer et al. 2011; van Velzen et al. 2011; Cannizzo et al. 2011) as evidence that relativistic jets can be triggered in quiescent massive black holes when an orbiting Sun-like star, owing to the cumulative effect of encounters with other stars (Frank & Rees 1977), gets too close to the black hole and is tidally disrupted².

Because the duration of the event is determined by the timescale at which the most bound material returns to pericenter forming an accretion disk (Evans & Kochanek 1989; Rees 1988; Rosswog et al. 2009; Ramirez-Ruiz & Rosswog 2009; Lodato et al. 2009; Guillochon et al. 2009), flaring black hole candidates in nearby galaxies

(fabio, jfg, jnaiman, enrico)@ucolick.org

¹ TASC, Department of Astronomy and Astrophysics, University of California, Santa Cruz, CA 95064, USA² Alternative models have also been considered (Socrates 2011; Krolik & Piran 2011; Quataert & Kasen 2011; Ouyed et al. 2011; Woosley & Heger 2011)

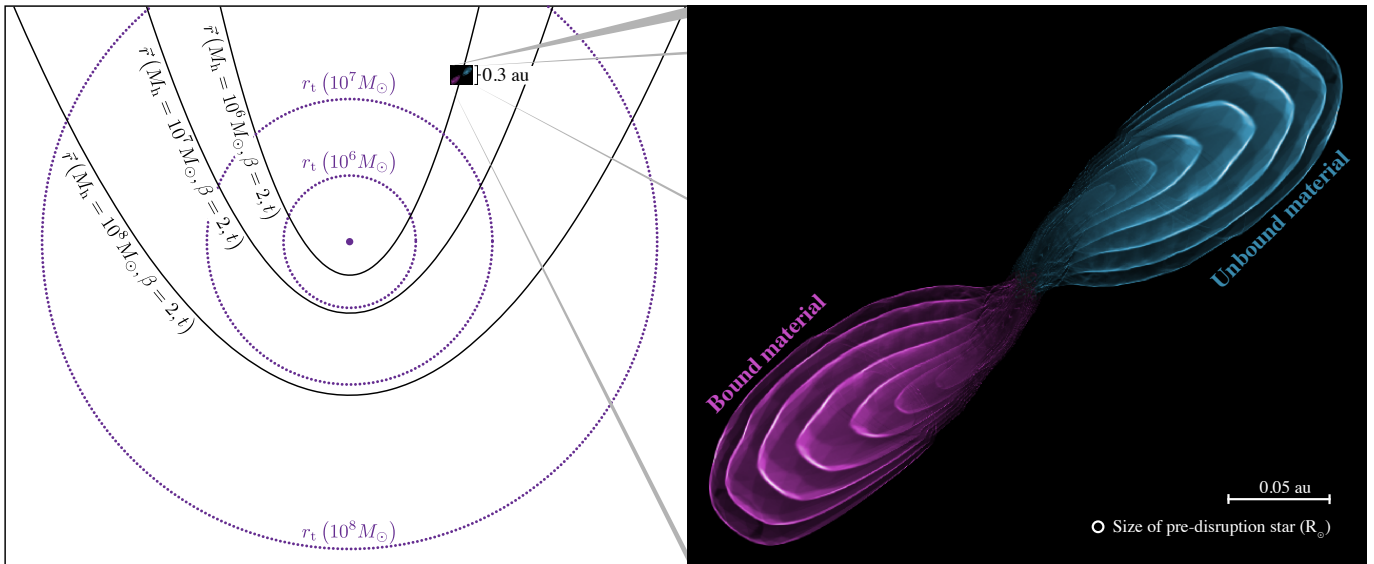


FIG. 1.— Diagram of the complete tidal disruption of a Sun-like star for several black hole masses. The left panel shows the system geometry for three black hole masses, $M_h = (10^6, 10^7, 10^8 M_\odot)$. Shown in black are the Newtonian orbital trajectories $\tilde{r}(M_h, \beta, t)$ for a $\beta = 2$ encounter, which we find to be fully disruptive in our hydrodynamical simulations. The tidal radius r_t for each M_h is shown by the dotted lines. Inset into the diagram along each orbital trajectory is a to-scale rendering of the orbital debris 4 hours after pericenter, generated from a single simulation with $M_h = 10^6 M_\odot$. The right panel shows a zoom-in of this debris, with contours showing constants values of ρe_h , where e_h is the specific binding energy to the black hole, with the contours ranging from 10^{12} ergs cm^{-3} to 10^{16} ergs cm^{-3} with logarithmic spacing. Material that is bound to the black hole after the encounter is shown in magenta, whereas unbound material is shown in cyan. The symmetry of the debris demonstrates the nearly symmetrical tide imposed by the black hole at closest approach.

offer the possibility of watching the evolution of a quasar-like object through many stages of its life in a time span of few months or years (e.g., Berger et al. 2012) rather than waiting the millions of years necessary to observe changes in extragalactic objects.

Much of our effort in this paper is therefore dedicated to study the dynamics of jets triggered by tidal disruption. Some of the questions at the forefront of our attention include the effects of the external medium and the degree to which the jet dynamics are modified by their energy injection histories. Because the mass accretion rate onto a black hole that is fed by tidal disruption is far from being steady and there is not a simple prescription for the surrounding density stratification, self-similar solutions fail to provide an accurate description of the jet dynamics, and thus simulations are required. The mass accretion history onto the black hole as well as the jet lifetime are calculated in Section 2 using detailed hydrodynamical simulations of the tidal disruption of Sun-like stars. The character of the external medium responsible for shaping the evolution and morphology of the jets is reviewed in Section 3. Detailed hydrodynamic calculations of the evolution of jets triggered by tidal disruption are presented in Section 4, together with a brief description of the numerical methods and the initial model. Finally, a tidal disruption model for the Swift 1644+57/GRB 110328A event is presented in Section 5, followed by a discussion on how the discovery of flaring candidates in nearby galaxies by *Swift* will help elucidate the demography of the dormant black hole population.

2. FEEDING RATES AND JET ACTIVITY FOLLOWING TIDAL DISRUPTION

2.1. Tidal Disruption Simulations

Our formalism for calculating the rate of mass return to the black hole \dot{M}_h after the disruption is identical to

the method presented in Guillochon et al. (2011), except for the initial conditions where we take the star to be a $1 M_\odot$ star described by a polytropic index $n = 3$ and an adiabatic equation of state with $\gamma = 5/3$. Our disruption simulations are performed using the FLASH hydrodynamics framework (Fryxell et al. 2000), which includes an adaptive mesh refinement scheme that permits the wide range of scales necessary to resolve the star and the debris streams simultaneously. During the disruption, the debris tails are adaptively refined based on their density relative to the maximum density in the simulation ρ_{max} at each time step, with a cutoff density for the lowest refinement level of 10^{-19} times the maximum density. All matter with $\rho > 10^{-3} \rho_{\text{max}}$ is refined to the highest level. The disruption is performed in a box that is several orders of magnitude larger than the initial star's radius of $r_* = R_\odot$, which is done to facilitate tracking of the tidal debris over long enough timescales for hydrodynamical effects to no longer play a major role in determining the distribution of mass as a function of binding energy.

2.2. Deriving $\dot{M}(M_h)$

To calculate the rate of mass return to the black hole \dot{M}_h as a function of the black hole mass M_h , we performed a single simulation of the disruption of a $1 M_\odot$ star by a $10^6 M_\odot$ black hole with impact parameter $\beta \equiv r_t/r_p = 2$, where r_t and r_p are the tidal and the periastron radius, respectively (see Figure 1). This encounter is deep enough to leave no surviving core (Guillochon & Ramirez-Ruiz 2012). To accurately model the disruption, we perform the simulation using a cubical volume with a basic grid of 8^3 cells (along each Cartesian coordinate axis), with a width of 4×10^{14} cm, and 16 levels of refinement, resulting in the initial diameter ($= 2R_\odot$) of the star being resolved by 90 grid cells. The shape of

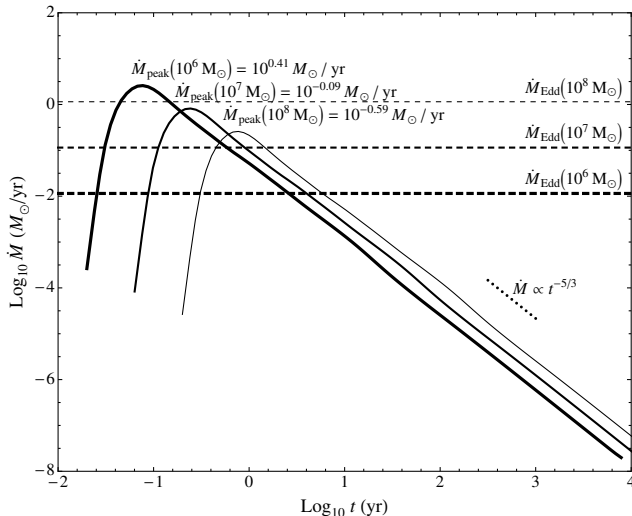


FIG. 2.— Rate of return of mass \dot{M} to the black hole following a $\beta = 2$ encounter, displayed as solid lines of decreasing thickness for increasing M_h . As the time of the encounter is independent of M_h at constant β , and the forces experienced along the trajectory are nearly identical, the rate of mass return simply scales with the spread of binding energy across the debris, $\dot{M} \propto M_h^{-1/2}$. The feeding rate rapidly converges to the predicted $t^{-5/3}$ power law, as shown by the short dotted line segment. Dashed lines show the Eddington feeding limit \dot{M}_{Edd} as a function of M_h , assuming an efficiency $\epsilon = 0.2$. The larger the mass of the black hole, the shorter the amount of time the black hole remains above a given \dot{M} . A disruption of a $1 M_\odot$ star by a $10^8 M_\odot$ black hole never exceeds the Eddington limit.

\dot{M}_h in the Newtonian approximation for full disruptions is only affected by the degree of symmetry in the tides (Guillochon et al. 2011) and the star’s initial density profile (Lodato et al. 2009; Ramirez-Ruiz & Rosswog 2009). As shown in Guillochon et al. (2011), tides are very symmetrical for black holes with $M_h \gtrsim 10^6 M_\odot$, with the maximum force difference between the near- and far-side of the star being 6% for a $\beta = 2$ encounter involving a $M_h = 10^6 M_\odot$, and even less for black holes of larger mass. Assuming that the shape of \dot{M}_h does not vary for black holes of mass $\geq 10^6 M_\odot$, $\dot{M}_h(M_h)$ can be related to our benchmark simulation via

$$\dot{M}_h(M_h, t) = \dot{M}_h(10^6 M_\odot, t') \left(\frac{M_h}{10^6 M_\odot} \right)^{-1/2} \quad (1)$$

$$t' = t \left(\frac{M_h}{10^6 M_\odot} \right)^{-1/2}, \quad (2)$$

where t and t' are the times since disruption for a black hole of mass M_h and our benchmark simulation, respectively (Evans & Kochanek 1989). Our simulation assumes that the typical disrupted star has a structure similar to that of the Sun, but stars of different masses and ages can have different degrees of central concentrations (Tout et al. 1996). Lodato et al. (2009) showed that for full disruptions the star’s initial density profile primarily affects \dot{M}_h at early times, but that all reasonable initial stellar profiles eventually lead to a power-law decay where $\dot{M}_h \propto t^{-5/3}$ at late times. Therefore, we assume that a typical disruption of a $1 M_\odot$ by a black hole of mass $M_h \geq 10^6 M_\odot$ can be reasonably modeled by a

single simulation using the above scalings, which yields the \dot{M}_h shown in Figure 2.

2.3. The Expected Jet Lifetime

The returning gas does not immediately produce a flare of activity from the black hole. First material must enter quasi-circular orbits and form an accretion torus (Ramirez-Ruiz & Rosswog 2009). Only then will viscous effects release enough binding energy to power a flare. Once the torus is formed, it will evolve under the influence of viscosity and radiative cooling, although the viscosity would have to be implausibly low (i.e. the usual viscosity dissipation time t_ν for a thick disk would be $\propto \alpha^{-1}$) for the bulk of the mass to be stored for longer than t_{peak} in a reservoir at $r \approx r_t$. After $t_\nu \ll t_{\text{peak}}$ the mass accretion rate would continue to fade as \dot{M}_h .

Little is known about the relation between jet production in supermassive accreting black holes and the state of their constituent accretion disks. However, an association between hot thick accretion flow with the strongest jets, as observed in binary black holes, is expected (e.g. Krolik & Piran 2012). It is the poloidal field protruding from the disk that is thought to drive the jet and because its strength increases with disk thickness, jets are expected to be stronger in thick disks than in thin ones (Meier et al. 2001). In GX 339-4, for example, a jet is produced when the X-ray source is in the low/hard state. In this state, the disk temperature is $T \sim 10^9 \text{ K}$, suggesting a thick disk. On the other hand, when the source enters the high/soft state (with a thin 10^7 K disk) the jet radio emission disappears to a level at least tens of times weaker (Fender et al. 1999). In what follows, we make the assumption that jets will be produced only when the accretion disk is geometrically thick and hot.

It is clear from Figure 3 that most of the debris would be fed to the black hole far more rapidly than it could be accepted if the radiative efficiency was high. As the disk material advects onto black hole, we thus assume a relativistic jet with $L_j(t) \propto \dot{M}_h(t)$ can be powered for as long as $\dot{M}_h(t) \gtrsim \dot{M}_{\text{Edd}}$.

3. PROPERTIES OF THE SURROUNDING MEDIUM

With the exception of our own galactic center and M31 where there are observational constraints on the extent of the confining gas on scales $r \leq 10 \text{ pc}$ within the nucleus (Quataert 2004; Garcia et al. 2010), little is known about the character of the medium surrounding black holes in the cores of inactive galaxies. We can thus place only somewhat model-dependent limits on the surrounding density and pressure structures. The jet’s advancement would be initially impeded near r_t , where the returning bound material forms a nearly hydrostatic envelope around the black hole (Loeb & Ulmer 1997), within which radiation pressure is dominant (region I in Figure 4). After the jet has broken free from the optically thick envelope, it passes through an extended region of steadily decreasing ambient pressure, whose properties are primarily shaped by stellar wind collisions within the dense core (region II in Figure 4). The most rapid drop in pressure probably occurs outside the dense core (region III in Figure 4), where mass whose gravitational field confines the ambient gas is likely to have an extended distribution, but with density rapidly decreasing

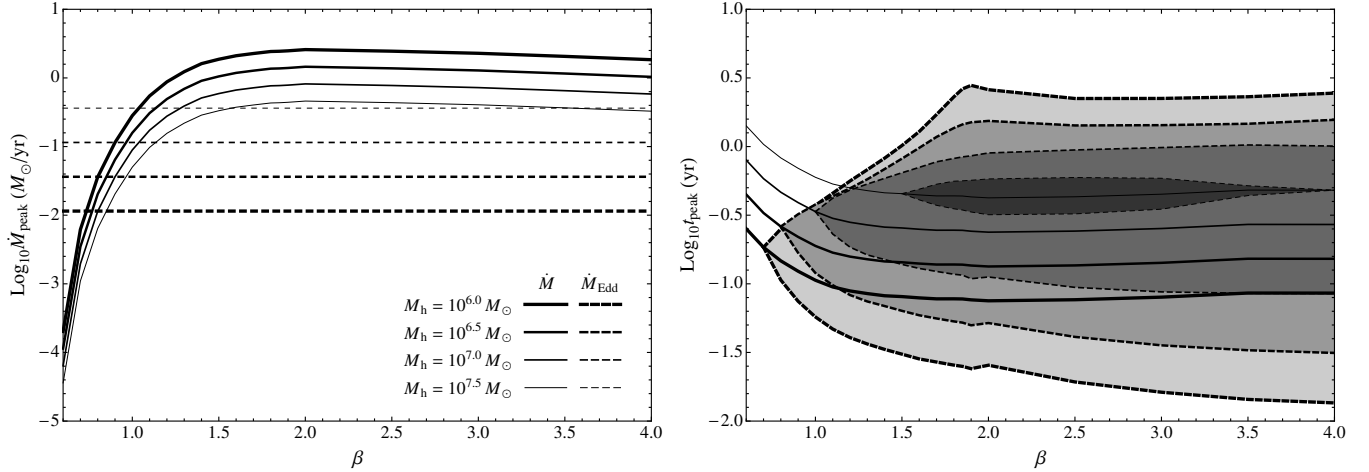


FIG. 3.— Peak accretion rate and time at which accretion peaks as a function of β for simulations of a $1M_{\odot}$ stellar disruption. The solid lines in the left panel show the peak accretion rate \dot{M}_{peak} as a function of β for several M_h , with the largest accretion rates being produced for $\beta = 2$ encounters. The corresponding Eddington accretion rates \dot{M}_{Edd} are shown as dashed lines. The right panel shows the time t_{peak} at which this peak accretion rate is achieved (solid lines of varying thickness), where t is measured relative to the time of pericenter. The span of time for which the black hole exceeds \dot{M}_{Edd} is shown by the gray contours which are bounded by the dashed curves. Disruptions occurring around black holes of larger mass peak at later times relative to pericenter, and exceed the Eddington threshold for a much shorter duration than their low-mass counterparts.

ing outwards. An understanding of the structure and evolution of jets triggered by tidal disruption can come only through knowledge of the properties of the material through which they propagate. For this reason, we now consider the surrounding density and pressure profiles in more detail.

3.1. Optically Thick Envelope

The structure of the optically thick, high entropy envelope formed as a result of the tidal disruption of a star by a massive black hole has been described by [Loeb & Ulmer \(1997\)](#). Their results, used as initial conditions in Section 4, are briefly described here. During the tidal disruption process, about half of the stellar material escapes on hyperbolic orbits with speeds $\sim 9500(M_h/10^6 M_{\odot})^{1/6}$ km/s, while the rest falls back onto the black hole. The bound gas, after pericenter passage, is on orbits which collide with the infalling stream near the original orbital plane at apocenter, giving rise to a shock which redistributes angular momentum ([Rosswog et al. 2009; Ramirez-Ruiz & Rosswog 2009](#)). The debris raining down would, after little more than its free-fall time, settle into a disk surrounded by a radiation-dominated envelope, whose inner radius is

$$r_t = r_* \left(\frac{M_h}{M_*} \right)^{1/3} \approx 2.15 \times 10^{13} \left(\frac{M_h}{10^6 M_{\odot}} \right)^{1/3} \text{ cm} \quad (3)$$

where $r_* \approx R_{\odot}$ and $M_* \approx M_{\odot}$.

The structure of such an envelope is simplified by the fact that a fully ionized gas dominated by Thomson opacity and radiation pressure tends to approach a uniform entropy state. Assuming hydrostatic equilibrium and an equation of state dominated by radiation pressure ($p \propto \rho^{4/3}$), the density stratification in the optically thick envelope can be written as

$$\rho_{\tau} = \frac{f M_*}{4\pi \ln(r_{\tau}/r_t) r^3}, \quad (4)$$

where f is the fraction of stellar material in the envelope and r_{τ} is the radius at which the envelope becomes optically thin, which for electron scattering opacity is given by

$$r_{\tau} \approx 1.7 \times 10^{15} \left(\frac{f M_*}{0.5 M_{\odot}} \right)^{1/2} \text{ cm}. \quad (5)$$

The density distribution derived in equation (4) is probably valid only at late times ($t \sim t_{\text{peak}}$), as the returning gas does not immediately produce a thick disk of radiation-dominated gas. First material must enter quasi-circular orbits. The bound orbits are initially very eccentric and the range of orbital periods is large. The orbital semi-major axis of the most tightly bound debris is

$$a \approx 10^3 \left(\frac{M_h}{10^6 M_{\odot}} \right)^{-1/3} \left(\frac{r_*}{R_{\odot}} \right) \left(\frac{M_*}{M_{\odot}} \right)^{-2/3} r_g, \quad (6)$$

and the period is

$$t_a \approx 7.3 \left(\frac{a}{10^3 r_g} \right)^{3/2} \left(\frac{M_h}{10^6 M_{\odot}} \right)^{-1/2} \text{ days}, \quad (7)$$

where $r_g \approx 1.5 \times 10^{11} (M_h/10^6 M_{\odot})$ cm is the gravitational radius. As a result of internal dissipation due to high viscosity or shocks, the debris raining down would, after one or two orbital periods ($t_a \ll t_{\text{peak}}$), form a highly elliptical disk surrounded by an extended atmosphere with a wide spread in apocentric distances, whose progressively increasing vertical scale is likely to be smaller than the one predicted by equation (5). For a $10^7 M_{\odot}$ black hole, t_a at $a \approx r_{\tau}$ is approximately 161 days while $t_{\text{peak}} \approx 89$ days.

3.2. Medium Shaped by the Interaction of Stellar Winds

Aside from our own galactic center and M31, we have no direct measurement of the gas content at sub parsec scales near massive black holes. The stellar density, however, is more well-known. After all, if the stars were

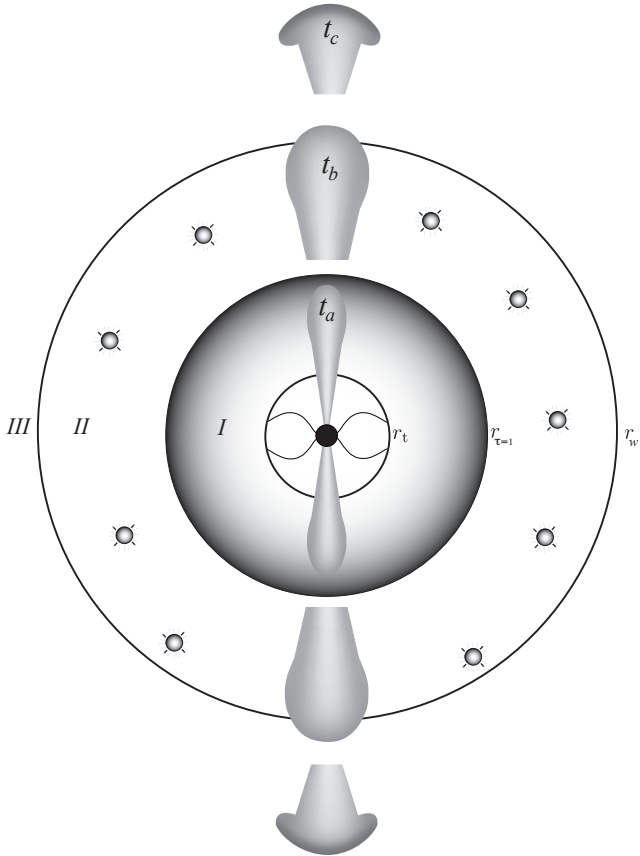


FIG. 4.— Schematic diagram of a relativistic jet propagating through the nucleus of a quiescent galaxy, illustrating the nomenclature of the external medium inferred to exist and the expected dynamical stages. Initially, a nearly hydrostatic envelope around the black hole, within which radiation pressure is dominant ($r \leq r_\tau$), will impede the advancement of the jet (region I). After emerging from the optically thick envelope, the jet is believed to move into a medium whose properties are primarily determined by the emanating stellar outflows within the nuclear cluster (region II). A jet emerging from the dense stellar core may pass through a region of steadily decreasing ambient pressure for up to several tens of parsecs (region III). Jet material travels along a channel of its own making. The speed with which the head of the channel advances into the surrounding medium is obtained by balancing the momentum flux in the jet against the momentum flux of the surrounding medium. A continuous flow of relativistic fluid supplies this region with mass, momentum, energy, and magnetic flux for as long as $t_a \lesssim t_{\text{Edd}}$. Information about a sizable decrease in power supply propagates into the jet at the internal sound speed (for $t \approx t_b$), reaching the head when the jet has traveled a further distance $r(t_c)$. Once these transient phase terminates, the bulk of the jet material expands freely.

not closely packed near the center of the galaxy, we would not have evidence for central black holes within quiescent galaxies. These same stars should provide mass winds, whose strength depends on the concentration of stars enclosed in the black hole's sphere of influence as well as the rates and velocity of the mass injection of those winds.

To determine the gas structures surrounding quiescent supermassive black holes, we follow the formalism developed by Quataert (2004), who modeled the distribution of hot gas around the central parsec of the galactic center under the assumption of spherical symmetry and an adiabatic equation of state. The one-dimensional hydrodynamical equations are also solved using FLASH (Fryxell et al. 2000), following the method described in Naiman

et al. (2012). The winds from the closely packed stellar members are assumed to shock and thermalize such that density and energy contributions can be treated as source terms in the hydrodynamical equations. In spherical symmetry, these equations can be written as (Holzer & Axford 1970):

$$\frac{1}{r^2} \frac{d}{dr} (\rho_a v r^2) = q(r) \quad (8)$$

$$\rho_a v \frac{dv}{dr} = -\frac{dp}{dr} - \frac{GM_h \rho_a}{r^2} - q(r)v \quad (9)$$

$$\frac{1}{r^2} \frac{d}{dr} \left[\rho_a v r^2 \left(\frac{v^2}{2} + \frac{c_s^2}{\gamma - 1} \right) \right] + \frac{\rho_a v GM_h}{r^2} = \frac{q(r)v_w^2}{\gamma(\gamma - 1)} \quad (10)$$

where the velocity, v , and density of the ambient medium, ρ_a , depend solely on r , and c_s is the sound speed of the gas.

At the central parsec of the galactic nuclei, gas is assumed to be supplied by winds which originate from massive stars. In our own galactic center, these stars include blue super giants each with mass loss rates $\dot{M}_w \approx 10^{-4} M_\odot \text{yr}^{-1}$ and wind speeds of $v_w \approx 600 - 1000 \text{ km s}^{-1}$ (e.g. Najarro et al. 1997). Here we use the term $q(r)$ to quantify the total rate of mass injection from the stellar winds:

$$\Sigma \dot{M}_w = \int 4\pi r^2 q(r) dr. \quad (11)$$

Following Quataert (2004) we set $q(r) \propto r^{-\eta}$ with $\eta = 0, 2, 3$ for $r \in [r_m, r_M]$ and $q(r) = 0$ otherwise. Different values of η correspond here to different mass injection distributions. A value of $\eta = 0$, for example, describes mass that is injected preferentially at large radii while $\eta = 3$ corresponds to equal mass injection for all radii within $[r_m, r_M]$. To uniquely specify $q(r)$, we must determine $\Sigma \dot{M}_w$ and η as well as $[r_m, r_M]$. For simplicity, we assume the central star cluster properties from Quataert can be scaled with the central black hole's mass, so that $[r_m, r_M] \propto M_h^{1/3}$ and $\Sigma \dot{M}_w \propto \Sigma N_* \propto M_h$.

Figure 5 shows the results of our simulations for different black hole masses. After many sound crossing times the flow settles into a steady state. Far away from the cluster, as expected, the flow is driven out by the aggregate influence of the stellar winds while interior to the cluster the gas is captured and accreted onto the central black hole. The stagnation radius, the boundary where the flow is divided between inflowing and outflowing, increases with the mass of the central black hole. As can be seen from Figures 5 and 6, the density stratification is strongly dependent on the black hole mass but nearly independent on the power-law assumed for the distribution of the mass injection (i.e. η).

The density distribution at small radii can be roughly described by $\rho_a \propto r^{-k}$ with $k \approx 1, 1.4, 1.5$ for $M_h = 10^6, 10^7, 10^8 M_\odot$ respectively. In the outer regions, the density is seen to rapidly converge to a $k = 2$ wind profile. Realistically, we would expect the ambient medium around the supermassive black hole to have a complex multiphase structure as inferred from models of the line-emitting region (Barai et al. 2011).

4. PROPAGATION OF JETS IN QUIESCENT GALACTIC NUCLEI

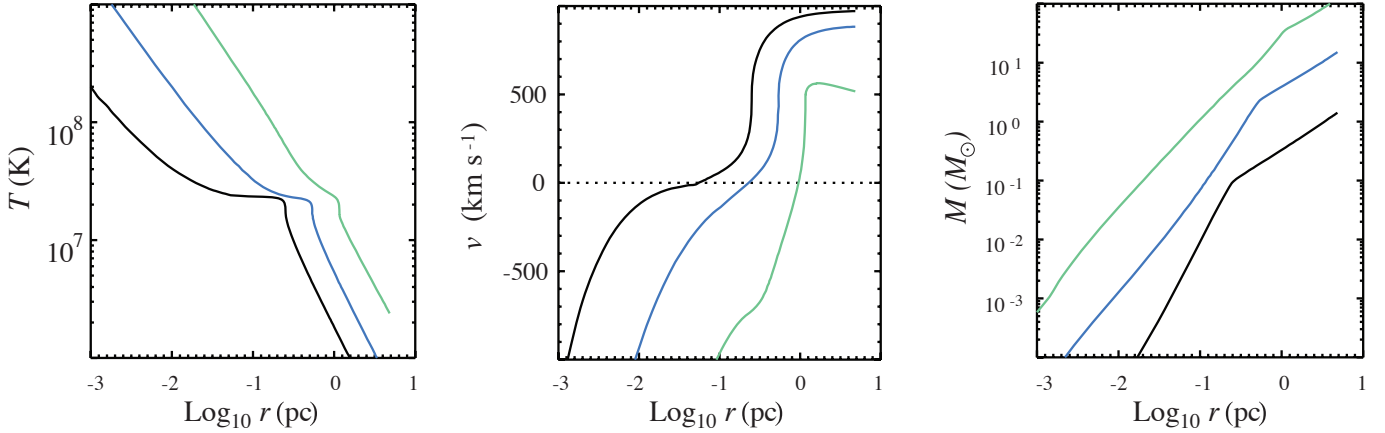


FIG. 5.— Comparison of the gas properties surrounding quiescent black holes of 10^6 (black curves), 10^7 (blue, dashed curves) and $10^8 M_\odot$ (green, dotted curves) for $\eta = 0$. The profiles for $10^6 M_\odot$ have been derived using the stellar wind properties observed in our own galactic nuclei, for which $\Sigma \dot{M}_w \approx 10^{-3} M_\odot \text{ yr}^{-1}$ and $v_w \approx 10^3 \text{ km s}^{-1}$ (Quataert 2004). In all cases, the flow at large radii (after a few sound crossing times) resembles that of a wind while interior to the mass injection region, the gas is captured and accreted onto the black hole. Fluid variables plotted from left to right are the temperature, $T(r)$, the flow velocity, $v(r)$, and the integrated mass profile, $M(< r) = \int_0^r 4\pi \rho(r') r'^2 dr'$.

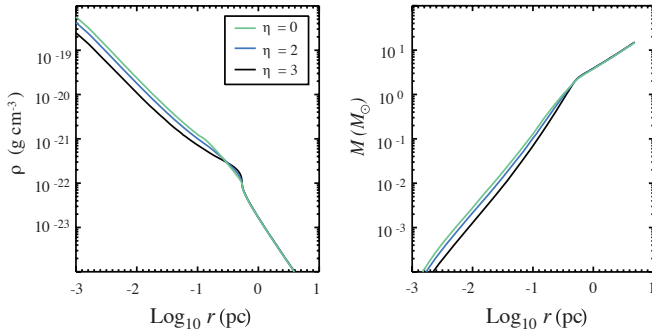


FIG. 6.— Densities and integrated mass profiles expected around a $10^7 M_\odot$ mass black hole for different mass injection distributions, parametrized here by $q(r) \propto r^{-\eta}$ for $r \in [r_m, r_M]$.

4.1. The Underlying Dynamics

A simple analytical argument can be used to understand the dynamical evolution of jets. Let us consider a cylindrically symmetric, relativistic jet moving through a stratified medium. As long as the flow is continuously injected, the head of the jet (or working surface) will have a double shock structure, composed by a forward and a reverse shock where, in the system of reference where the contact discontinuity is at rest, the ambient medium and the jet material respectively are decelerated and heated, transforming kinetic into thermal energy.

The speed v_h with which the head of the channel advances into the surrounding medium is obtained by balancing the momentum flux in the shocked jet material against that of the shocked surrounding medium, measured in the frame comoving with the advancing head (e.g. Begelman & Cioffi 1989; Ramirez-Ruiz et al. 2002; Matzner 2003; Bromberg et al. 2011; Lazzati et al. 2011; Metzger et al. 2012):

$$\rho_j h_j \Gamma_j^2 \Gamma_h^2 (v_j - v_h)^2 + p_j = \rho_a h_a \Gamma_a^2 v_h^2 + p_a, \quad (12)$$

where $\rho_{j,a}$, $h_{j,a}$, $\Gamma_{j,a}$, and $p_{j,a}$ are the mass density, specific enthalpy, Lorentz factor and pressure of the jet and ambient medium respectively, and $v_{j,h}$ is the velocity of the jet and the advancing head (where $u = \Gamma\beta = \Gamma v/c$ is the proper fluid velocity and $h_a \simeq 1$). If v_h is supersonic

with respect to the ambient gas, $p_{a,j}$ can be neglected and equation (12) gives

$$v_h = v_j \left[1 + \left(\frac{\rho_a}{\rho_j h_j \Gamma_j^2} \right)^{1/2} \right]^{-1}. \quad (13)$$

The resulting flow pattern will depend crucially upon the jet Mach number and the density ratio between the jet and the given ambient medium. When the jet density significantly exceeds the ambient density, $v_h \approx v_j$.

A relativistic jet emerging from the galactic core will pass through a region of steadily decreasing ambient density for up to several tens of parsecs (Figure 4). Even if the jet is confined, this decrement in density will result in an increase in cross section, and the degree of collimation $\theta = s/r$ will either decrease or increase, depending on whether the size of the evacuated channel s increases more or less rapidly than r . This indicates that the dynamics of the expanding jet is expected to be modified by changes in collimation and can not be properly captured by spherically symmetric solutions. These difficulties motivate consideration of the hydrodynamical confinement in axisymmetric numerical calculations, to which we now turn our attention.

4.2. Numerical Methods and Initial Model

The propagation of relativistic jets triggered by the tidal disruption of stars in quiescent supermassive black holes is studied here by using the adaptive mesh refinement code *Mezcal*. The code solves the special relativistic hydrodynamics (SRHD) equations in two-dimensional spherical (polar) coordinates. The *Mezcal* code integrates the SRHD equations by using a second-order upwind scheme. The equation of state, relating enthalpy to pressure and density, assumes an adiabatic index $\gamma = 4/3$. A detailed description of the SRHD version of the *Mezcal* code is presented in De Colle et al. (2012a) together with a series of standard tests³.

³ The code is routinely used to calculate the dynamics and appearance of relativistic, impulsive flows, thought to accurately de-

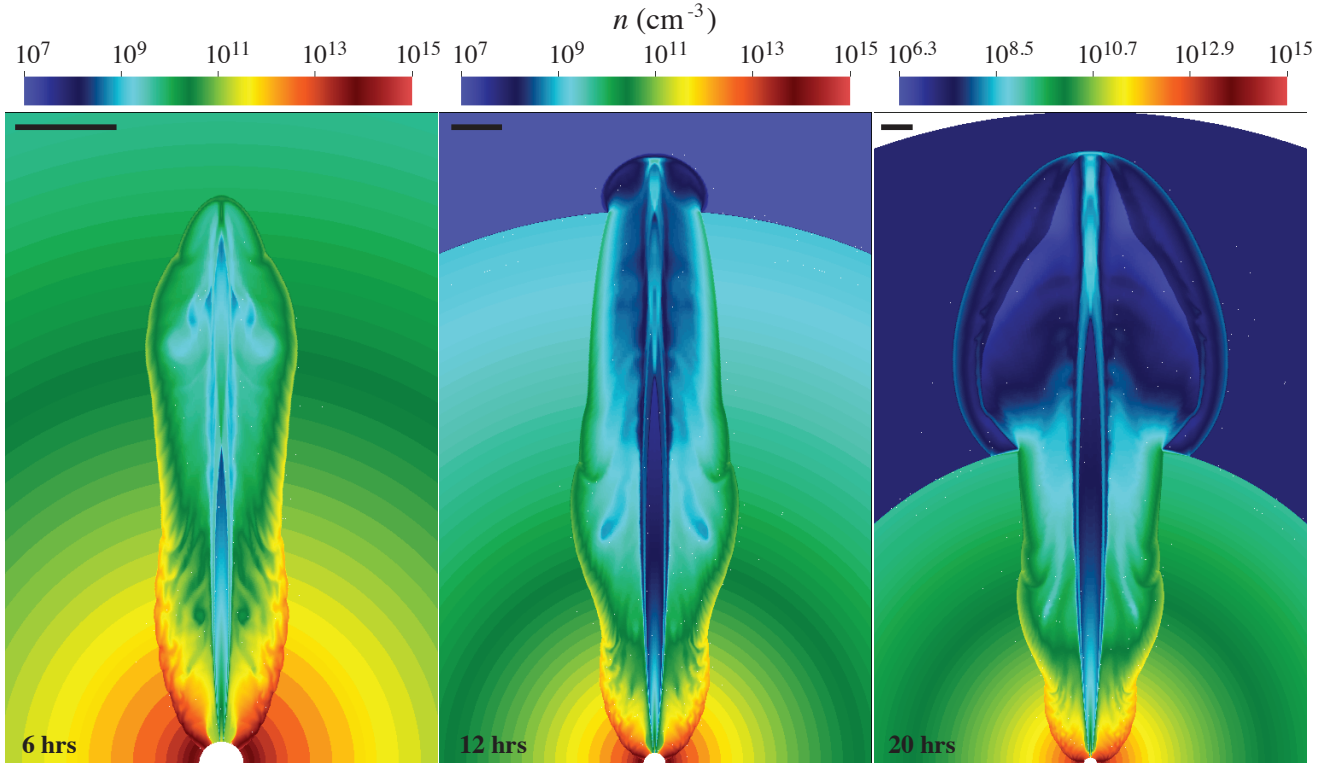


FIG. 7.— Propagation of a relativistic jet through the envelope of high-entropy gas that might form around a massive black hole of mass $M_h = 10^7 M_\odot$ as a result of the tidal disruption of a star. Shown are logarithmic density cuts in cm^{-3} . Evolutionary ages after injection (assumed here to be at $t \sim t_{\text{peak}}$) are indicated in each frame together with a corresponding size 10^{14} cm scale bar. The jet is initialized at $r_0 = r_t = 4.6 \times 10^{13}$ cm with $\Gamma = 10$ and $\theta_0 = 0.1$. The jet luminosity, characterized by $\epsilon_j = 0.1$, is injected as 20% thermal and 80% kinetic. The envelope is characterized by $r_\tau = 10^{15}$ cm, corresponding to $f = 0.4$. For $r > r_\tau$, the density and pressure are assumed to be constant with $\rho_a = 10^{-2} \rho_a(r_\tau)$ and $p_a = p_a(r_\tau)$. The size of the computational domain was $(2r_\tau)^2$. The simulation employs a two-dimensional spherical adaptive mesh grid, with 100×40 cells along the r and θ directions at the coarsest level, and 5 level of refinement, with a maximum resolution of $\Delta r = 1.3 \times 10^{12}$ cm and $\Delta \theta = 2.5 \times 10^{-3}$ rad.

Common to all calculations is the initiation of a conical jet with an initial opening angle θ_0 and uniform velocity $u_0 = \Gamma_0 \beta_0$, with matter injected along the symmetry axis at the inner boundary of the computational domain $r = r_0$. The luminosity of the jet is assumed here to follow the mass accretion rate, $L_j(t) = \epsilon_j c^2 \dot{M}_h(t)$. This relation together with mass conservation determines the density of the jet, $\rho_j(r_0)$, at the injection boundary. Given the large range in scales, the propagation of the jet in the optically thick envelope ($r \leq r_\tau$) and its subsequent expansion through the medium shaped by the interaction of massive stellar winds ($r \leq r_M \approx 10^3 r_\tau$) are studied separately.

4.3. Jet Propagation in the Optically Thick Envelope

The existence of a steady, spherical, optically thick envelope around the black hole should be regarded as an extreme assumption as its extension and structure will be modulated at a variable rate by fallback. The envelope starts to form when the most tightly bound debris fall back. Our stellar disruption simulation (Section 2) shows that the first material returns at a time t_a , with an infall rate of about $\dot{M}_a \approx 10^{-4} M_\odot \text{yr}^{-1} \leq \dot{M}_{\text{Edd}}$ (Figure 2). The infall rates are expected to increase, relatively steadily, for at least tens of orbital periods, before the

majority of the bound material rains down at $t \approx t_{\text{peak}}$. Once the envelope is formed, it will evolve under the influence of viscosity, radiatively cooling and time dependent mass injection from both the jetted outflow and the angular momentum redistribution region.

To study the evolution of the relativistic jet in the optically thick region, we assume, for simplicity, the envelope to be fully formed ($t \sim t_{\text{peak}}$) and accurately described by the steady, spherical hydrostatic solutions presented in Section 3.1. In addition, since the jet head breaks out of the envelope after only a time $r_\tau/c \ll t_{\text{peak}}$, the jet power is assumed to be steady during this phase with $L_j \approx \epsilon_j \dot{M}_{\text{peak}} c^2$.

Snapshots of detailed hydrodynamic simulations of the evolution of the jet through the optically thick envelope are presented in Figure 7, where the density maps of the expanding jet at various times after t_{peak} in its hydrodynamical evolution are plotted. Initially, the low-density jet is unable to move the envelope material at a speed comparable to its own and thus is abruptly decelerated. Most of the energy output during that period is deposited into a cocoon surrounding the jet, in which the energy supplied by the jet exceeds that imparted to the swept-up envelope material by a factor β_h^{-1} . In the cocoon region the jet and ambient medium remain separated by a contact discontinuity where shearing instabilities are prominent. The cocoon region exhibits two important

scribe the evolution of gamma ray burst afterglows (De Colle et al. 2012b).

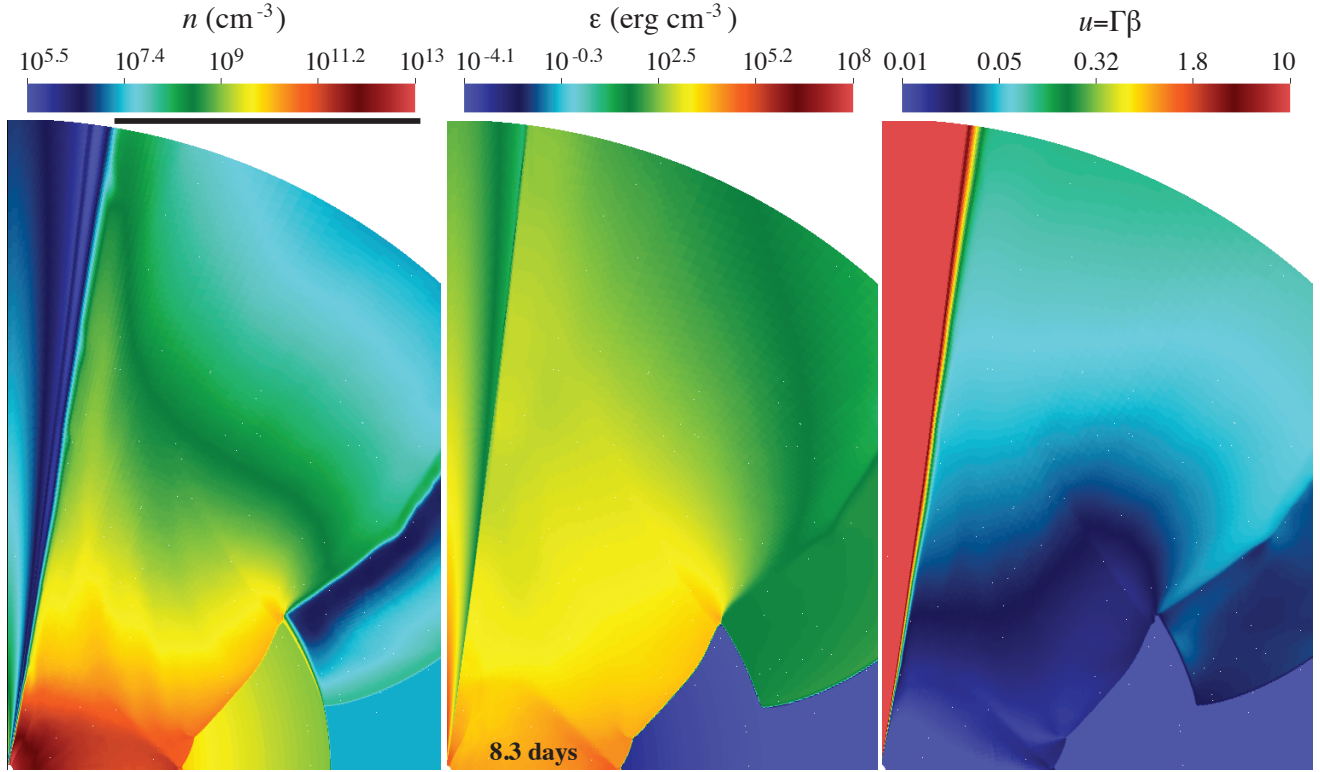


FIG. 8.— The expansion of the cocoon material ~ 7.9 days after the jet head in Figure 8 has broken free from the optically thick envelope. Shown are the density, internal energy and velocity at 8.3 days after injection (assumed here to be at $t \sim t_{\text{peak}}$). A 10^{14} cm size scale bar is shown in the left panel.

dynamical effects (e.g. Bromberg et al. 2011). First, it forms a weak shock that moves laterally at the relativistic internal sound speed, and second, it acts to partially collimate the jet itself. As the jet expands further into the envelope, the drastic density drop permits the jet head to accelerate to velocities close to the speed of light ($\beta_h \approx 1$). Thus, if it is a general property that the jet becomes relativistic near the boundary of the envelope, the outer edge of the envelope is reached in a crossing time $\approx r_\tau / (c\beta_h\Gamma_h^2)$ as measured by an observer along the line of sight.

After the jet has broken free from the envelope region, the fraction of relativistic plasma injected into the cocoon will be much reduced as the jet accelerates and $\beta_h \approx 1$. The amount of energy that accumulated in the cocoon while the jet was advancing sub-relativistically is

$$E_c \approx 10^{50} \bar{\beta}_h^{-1} \left(\frac{r_\tau}{10^{15} \text{cm}} \right) \left(\frac{L_j}{10^{46} \text{erg s}^{-1}} \right) \text{erg}, \quad (14)$$

where $r_\tau / \bar{\beta}_h$ is the envelope traversal time and $\bar{\beta}_h$ is the average speed of the jet head. The energy accumulated in this phase is thus larger than the binding energy of the envelope⁴. At the radius $\approx r_\tau$ where the head of the jet starts to advance relativistically, the volume of the region incorporated into the cocoon is related to both the jet and cocoon expansion velocities by $V_c \approx (\pi/3)r_\tau^3(\beta_c/\beta_h)^2$. Unlike the jet, this cocoon material does not have a relativistic outward motion, although it has a relativistic internal sound speed. At first an

elongated bubble (since pressure balance may never be reached within a radiation-dominated isentropic atmosphere) will be inflated, which can expand most rapidly along the rotation axis and will eventually unbind the envelope (Figure 8). Even under the extreme assumption that the envelope is fully formed at $t \approx t_{\text{peak}}$, the energy deposited by the jet is expected to eject most of the envelope material in the optically thick region. Thus, passage through this region cannot significantly alter the jet launching conditions or enhance collimation.

4.3.1. Internal Shocks

Instead of assuming the jet to be a steady outflow, here we suppose that it is irregular on timescales much shorter than t_{peak} . For instance, if the Lorentz factor in the outflowing collimated ejecta varied by a factor of more than 2, then the shocks that developed when fast material overtook slower material would be internally relativistic (Rees & Meszaros 1994). Dissipation would then take place whenever internal shocks developed in the ejecta, which can then be reconverted into energetic particles and radiation (the jet may also lose energy as it propagates through the photon field of the accretion disk). Internal shocks generated either as a consequence of fluctuations at the source (e.g. Kobayashi et al. 1997; Ramirez-Ruiz & Lloyd-Ronning 2002) or arising from the development of large-amplitude instabilities provide an attractive explanation for the large scale variability seen in the Swift 1644+57/GRB 110328A event (Bloom et al. 2011; Burrows et al. 2011).

To illustrate the basic idea, suppose that two blobs of equal mass, but with different Lorentz factors Γ_i and Γ_j

⁴ provided that $M_h < 10^8 M_\odot$, above which the majority of main sequence stars are swallowed whole.

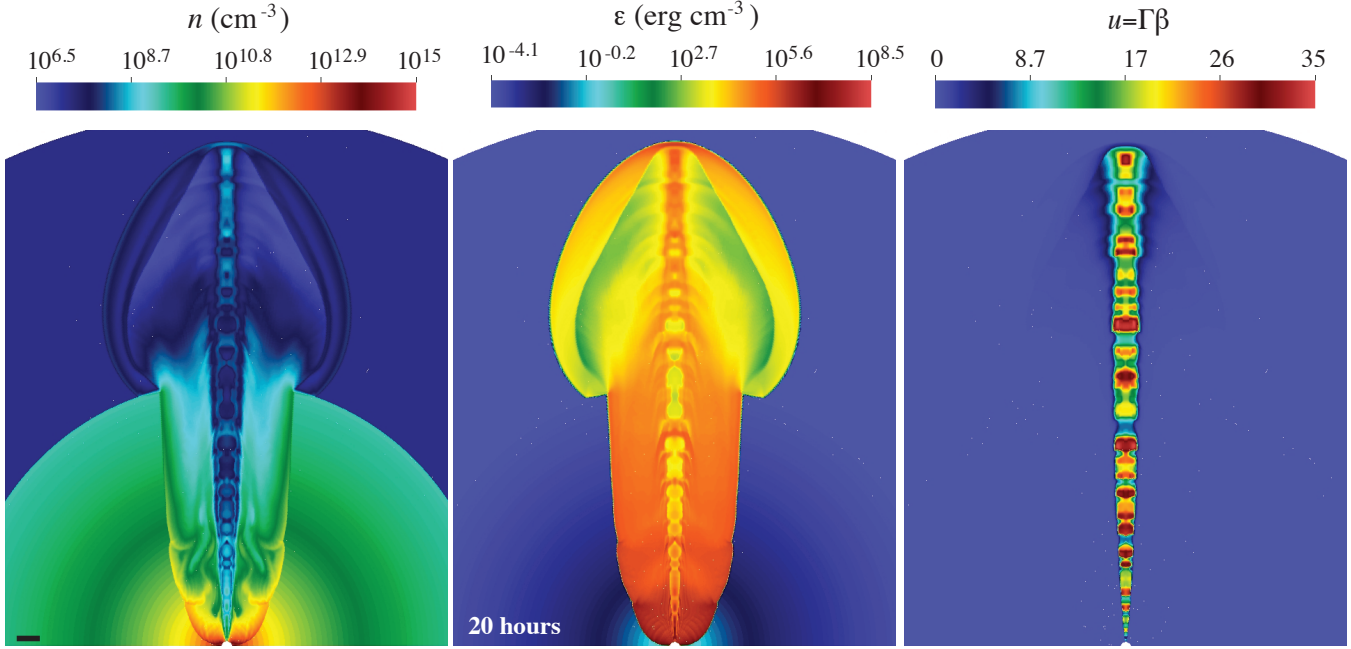


FIG. 9.— Propagation of a relativistic jet with an imposed random variation in both time, $\delta t \in [10^2, 10^3]$ s, and velocity, $\Gamma \in [2, 20]$. The jet average properties are the same as in Figure 7. Shown are the density, internal energy and velocity at 20 hours after injection (assumed here to be at $t \sim t_{\text{peak}}$). A 10^{14} cm size scale bar is shown in the left panel.

(with $\Gamma_i > \Gamma_j \gg 1$) are ejected at times t_1 and t_2 , where $t_2 - t_1 = \delta t$. In the case of highly relativistic ejecta, the shock develops after a distance of order

$$r_i \approx c \delta t \frac{2\Gamma_i^2 \Gamma_j^2}{\Gamma_i^2 - \Gamma_j^2} \approx 6 \times 10^{15} \left(\frac{\delta t}{10^3 \text{s}} \right) \left(\frac{\Gamma_j}{10} \right)^2 \text{ cm}. \quad (15)$$

The reconversion of bulk energy can be very efficient: when the two blobs share their momentum, they move with $\Gamma_{ij} = \sqrt{\Gamma_i \Gamma_j}$, so the fraction of the energy dissipated is

$$\epsilon_i = \frac{\Gamma_i + \Gamma_j - 2\sqrt{\Gamma_i \Gamma_j}}{\Gamma_i + \Gamma_j}. \quad (16)$$

High efficiency does not, therefore, require an impact on matter at rest; all that is needed is that the relative motions in the comoving frame be relativistic.

The evolution of a non-steady relativistic jet with randomly varying Lorentz factor Γ (between 2 and 20) over a range of timescales $10^2 \text{s} \lesssim \delta t \lesssim 10^3 \text{s}$ is shown in Figure 9. The average parameters of the jet are chosen so that they are similar to those displayed in Figure 7. Compared to Figure 7, significant structural differences along the evacuated channel appear when faster material catches up with slower material and a strong shock forms. An internal shock in the relativistic jet will move with a Lorentz factor of up to $\Gamma_{ij} \approx 10$, and the emitting material behind the shock will be subject to a large Doppler boost. Dissipation, to be most effective, must occur when the envelope is optically thin, i.e. $r_i \gtrsim r_\tau$ (Figure 9).

The deceleration of the working surface allows slower ejecta to catch up with the head of the jet, replenishing and reenergizing the reverse shock and boosting the momentum in the working surface. Since the efficiency of converting bulk motion to radiation in an internal shock depends on the difference between Γ 's, the fact that the

working surface is decelerating ($\beta_h \lesssim 1$) implies that the efficiency will be much higher than in the standard case where Γ is assumed to fluctuate by a factor of a few within the jet and among blobs on a typical timescale $\delta t \gtrsim r_g/c \approx 50(M_h/10^7 M_\odot) \text{ s}$.

4.4. Jet Propagation in the Stellar Wind Region

We now turn our attention to the evolution of the jet as it expands through the large scale environment of the galactic nuclei where the density stratification is thought to be regulated by the interaction of winds from the surrounding massive stars. The deceleration of the jet within this region gives rise to the non-thermal, long-lived radio emission observed in the Swift 1644+57/GRB 110328A event (Zauderer et al. 2011; Berger et al. 2012). The density profile within this region is taken from the simulations of the interacting stellar winds described in Section 3.2 and shown in Figures 5 and 6. The power of the jet is assumed to follow the mass feeding rate, $L_j(t) = \epsilon_j c^2 \dot{M}_h(t)$, with $\dot{M}_h(t)$ taken from the results of the tidal disruption simulations presented in Section 2 and Figure 2.

Little is known about the relation between jet production in the more massive accreting black holes and the state of their constituent accretion disks. However, a similar association of hot thick accretion flows with the strongest jets as seen in binary black holes is expected. Motivated by this, we assume that strong relativistic jets preceding tidal disruption are only triggered when $\dot{M}_h(t) \gtrsim \dot{M}_{\text{Edd}}$. The properties of these jets are thus severely constrained by the mass feeding rate history. The emitted radiation is an observable diagnostic which provides constraints on the processes occurring at their point of origin.

The propagation of a jet injected at the onset of the super-Eddington accretion phase over successive decades

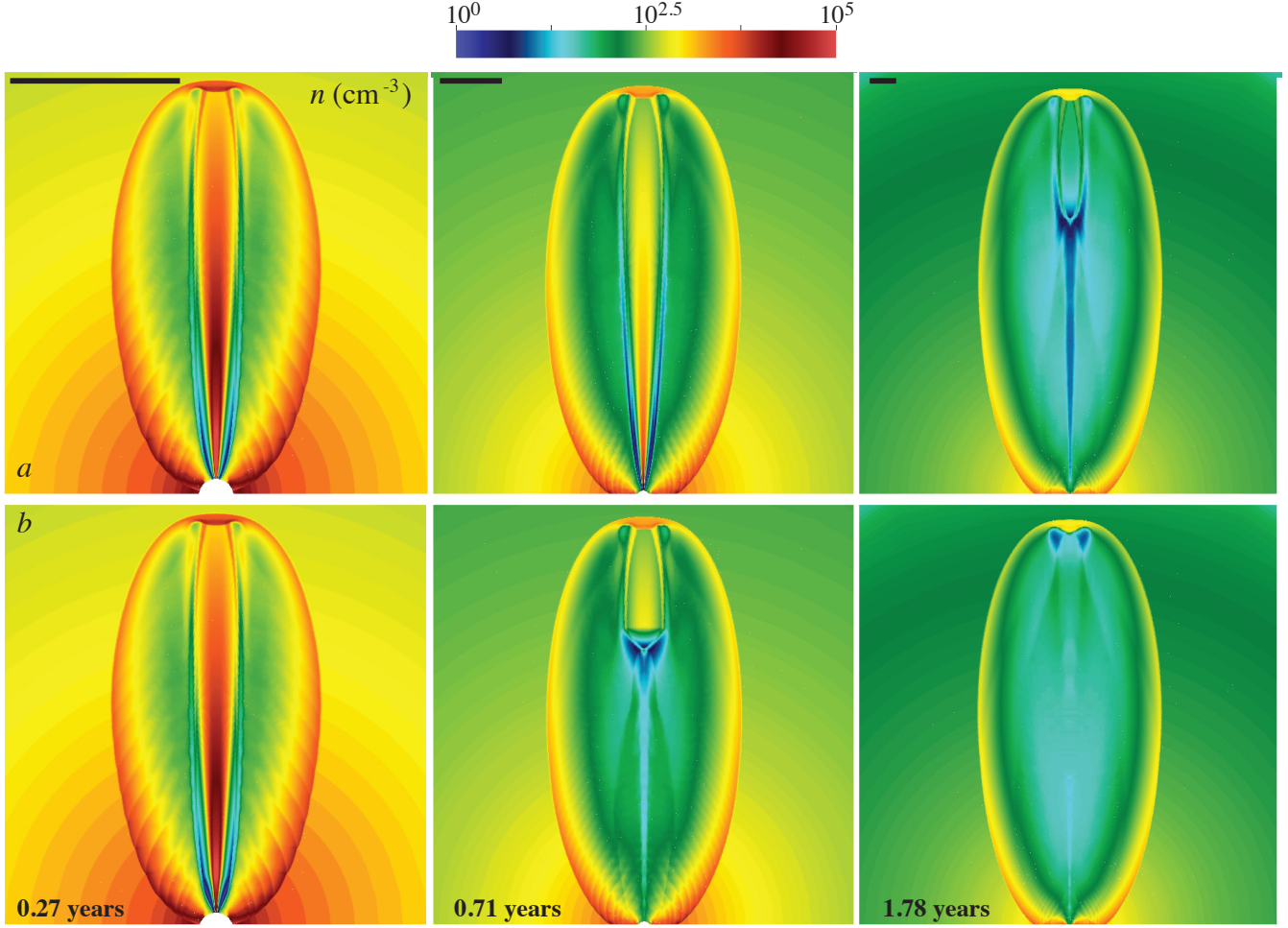


FIG. 10.— Propagation of a relativistic jet through the sub-parsec region shaped by the interaction of massive stellar winds that might be present in the nucleus of a massive black hole of mass $M_h = 10^7 M_\odot$. Shown are logarithmic density cuts in cm^{-3} . Evolutionary ages after injection are indicated in each frame together with a corresponding size 10^{17} cm scale bar. The jet is initialized at $r_0 = 10^{16}$ cm with $\Gamma = 5$ and $\theta_0 = 0.1$. The jet luminosity, characterized by $\epsilon_j = 0.1$, is injected as 20% thermal and 80% kinetic. The external density is taken from the simulations of the interacting stellar winds shown in Figures 5 and 6, while the jet luminosity is assumed to follow the mass feeding rate $\dot{M}_h(t)$ for as long as $\dot{M}_h(t) \gtrsim \dot{M}_{\text{Edd}}$ (case *a*). In case *b*, the jet luminosity is halted when $\dot{M}_h = \dot{M}_{\text{peak}}$. Cases *a* and *b* have been constructed to illustrate the effect of the $\propto t^{-5/3}$ injection phase on the jet dynamics. The simulations employ a two-dimensional spherical adaptive mesh grid, with 400×4 cells along the r and θ directions at the coarsest level, and with 10 level of refinement, corresponding to a maximum resolution of $\Delta r = 1.3 \times 10^{13}$ cm and $\Delta \theta = 7.7 \times 10^{-4}$ rad in the radial and azimuthal direction respectively. With this resolution, the azimuthal extent of the jet is resolved with ~ 65 cells at the finest level of refinement.

in radius ranging from 10^{-2} pc to 1 pc is shown in Figure 10 for $M_h = 10^7 M_\odot$. Two illustrative cases are depicted. In case *a*, the jet power increases with time to achieve a maximum at $t = t_{\text{peak}} \approx 0.27$ yrs, it then subsequently decreases as $\sim t^{-5/3}$ until it is finally halted at the time when $\dot{M}_h(t) < \dot{M}_{\text{Edd}} \approx 0.71$ yrs. In case *b*, the injection history is the same until the jet power is prematurely halted at $t = t_{\text{peak}}$. Figure 11 shows the corresponding schematic world-lines of the bow shock evolution for the two illustrative cases depicted in Figure 10.

As seen in Figure 10, the jet evacuates a channel out to some location where it impinges on the surrounding medium. A continuous flow of relativistic fluid emanating from the nucleus supplies this region with mass, momentum and energy. The jet, unable to move the surrounding material at a speed comparable to its own, is decelerated and, as a result, most of the energy output during that period is deposited into a cocoon surrounding the jet. As a first approximation, evolution of

the cocoon's shape is governed both by the advance of the head and by the cocoon's own pressure-driven sideways expansion into the surrounding medium. Heavy jets therefore propagate almost ballistically and are naturally surrounded by small cocoons. Light jets have large cocoons and, as seen in Figure 10, can be confined by the pressure of the shocked material.

The cocoon will effectively collimate the jet (Bromberg et al. 2011) as long as

$$\rho_j h_j \Gamma_j^2 / \rho_a < \theta_0^{-4/3}. \quad (17)$$

where $\rho_j h_j \Gamma_j^2 / \rho_a$ gives the ratio between the jet's energy density and the rest-mass energy density of the surrounding medium at the location of the head. Collimation is then seen to increase with decreasing k for $k \leq 2$. When $k = 2$ the jet's head velocity is constant and consequently most of the energy flowing into the cocoon can not effectively counterbalance the jet's expansion. The density

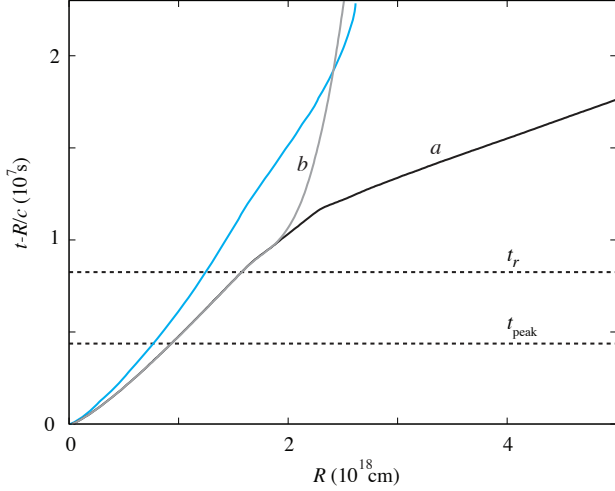


FIG. 11.— Schematic space time diagram in source frame coordinates for the two cases depicted in Figure 10. The axes (logarithmic) are r versus $t - (r/c)$, where t is time measured in the source frame, and is zero when the star is initially disrupted. In this plot, light rays are horizontal lines. Shown are the position of the bow shock as a function of time. In case a , $L_j \propto \dot{M}_h(t)$ for $t \leq t_{\text{Edd}}$. In case b , the jet luminosity is halted at $t = t_{\text{peak}}$. Information about the abrupt change in the feeding rate (at $t \gtrsim t_{\text{peak}}$) propagate into the jet at the internal sound speed and are communicated to the jet by an inward propagating rarefaction wave that reaches the jet head at $t_r \gg t_{\text{peak}}$. The blue solid line shows, for comparison, the evolution of the working surface as predicted by equation (12) for case b under the assumption of an non-evolving jet opening angle.

profile $\rho_a \propto r^{-k}$ in the stellar wind mass injection region (region II in Figure 4) varies from $1.4 \lesssim k \lesssim 2$ with increasing r for a $M_h = 10^7 M_\odot$ and, as a result, the cocoon's pressure is expected to collimate the jet and decrease its opening angle. This is clearly illustrated in Figure 11 in which the results of the simulations are directly compared with the evolution of the working surface as predicted by equation (13). In a jetted source like Swift 1644+57/GRB 110328A, the expansion of the working surface within the gas on scales $r \leq 1$ pc is clearly incompatible with that predicted on the assumption of a constant jet opening angle.

If the jet were suddenly to turn off (in case a this occurs at $t = t_{\text{Edd}}$ while in case b at $t = t_{\text{peak}}$) it would be preceded by the collapse of the jet channel which, suddenly evacuated, would be filled in on the transverse sound crossing time by whatever material happened to surround it. This ambient or cocoon material could be driven into the jet channel at the internal sound speed (Figure 10). After the evacuated channel collapses, a cylindrical rarefaction wave will propagate along the jet channel, reaching the head at $t = t_r \gg t_{\text{peak}}$ when the jet has traveled a much larger distance (r_r) than when it was initially turned off. This is followed by a series of compression and rarefaction waves of decreasing amplitude. In case a , the inclusion of the $\propto t^{-5/3}$ injection phase produces only a small change in t_r . This is clearly illustrated in Figure 12, where we have plotted the total internal energy available at the working surface. After the rarefaction wave reaches the jet head, which is observed to take place at comparable times in both of the cases depicted in Figure 10, the available internal energy drops although it does so less abruptly in case a where the jet continues to be powered until t_{Edd} . The inten-

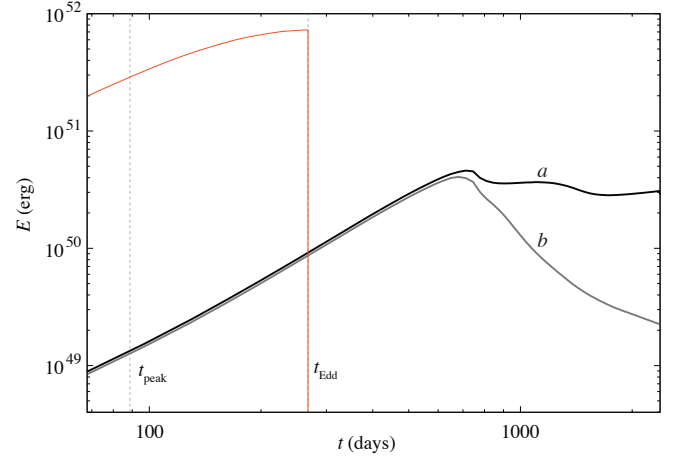


FIG. 12.— The evolution of the total internal energy available at the working surface for the two cases depicted in Figure 10. Also shown (red line) is the cumulative energy injected by the relativistic jet as a function of time. After rarefaction wave reaches the jet head, which occurs at similar times in both cases, the available internal energy drops although it does so more abruptly in case b where the jet power is halted at $t_{\text{peak}} < t_{\text{Edd}}$.

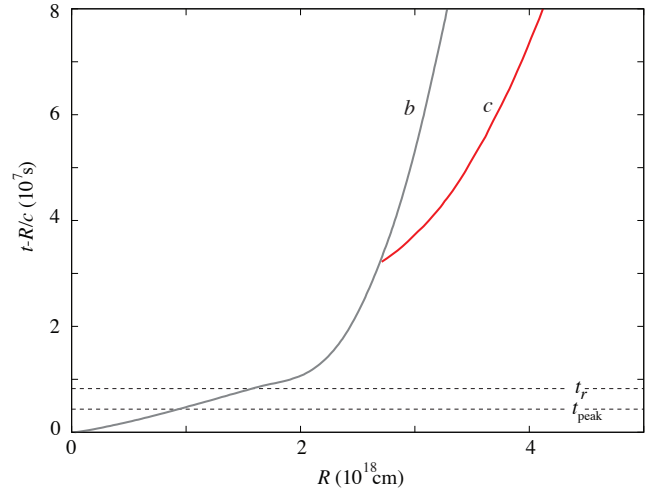


FIG. 13.— Schematic space time diagram in source frame coordinates illustrating the position of the bow shock. The simulation is the same as in Figure 11 for case b (jet injection stopped at $t = t_{\text{peak}}$) but with significant energy injection arising from slowly moving material (case c).

sity of the radiation from the radio-emitting electrons which have recently emerged from the hot spot rapidly decreases after a time $t_r \gg t_{\text{peak}}$, which corresponds to a time $\approx r_r / (c\beta_h \Gamma_h^2)$ as measured by an observer along the line of sight.

When the jet becomes free at $t \gtrsim t_r$, the necessary condition for the jet to remain in pressure balance with its surroundings is no longer satisfied and strong shocks are driven into the jet. As a result, the contact discontinuity and the forward shock are abruptly decelerated. This deceleration allows ejecta to catch up and pass through a reverse shock just inside the contact discontinuity, increasing the dissipated internal energy at the shock front (Figure 13) and in principle giving rise to a longer-lived afterglow than that predicted by the communication delay between the working surface and the base of the jet.

5. DISCUSSION

5.1. *The Properties of Jets Triggered by Tidal Disruption*

Quiescent black holes appear to be capable of producing directed flows of relativistic matter. Given the twin requirements of super Eddington luminosity and short flaring timescales, the currently favored models involve the disruption of a star with the subsequently accreted debris providing the required luminosity. Here we examine, within this model, the consequences of assuming a relation between jet production and the state of their constituent accretion disks. In those sources that display jets, production of the jet should only occur when the disk is in a hard accretion state and not when the disk emission is soft. Testing this prediction in quiescent galactic nuclei, as argued in Section 5.3, will require statistical studies because the typical jet production duty cycle time is expected to be thousands of years. Confirmation of this effect will provide additional evidence that accretion states similar to those in binary black holes also should exist in supermassive black holes. As we show in Section 5.2, many of the observed properties the Swift 1644+57/GRB 110328A event can be understood as resulting from a hot accretion flow, driven into a previously quiescent supermassive black hole, which is then subsequently collimated into a pair of anti-parallel jets. If we were to venture a general classification scheme for tidal disruption jets, we would obviously expect the black hole mass, the rate at which the gas is supplied to the black hole, the angular momentum of the black hole, the flow velocity and the orientation relative to our line of sight to be the essential parameters.

Most of the radiation we receive is reprocessed by matter quite distant from the black hole. The fact that jets are detectable at all means that some re-randomization of kinetic energy and re-acceleration of particles must be occurring along their length to counteract radiation and adiabatic losses. Under the assumption that these prime movers are able to form collimated, relativistic outflows, the observable effects of the two major radiating regions, the working surface and internal shocks, are studied. This leads to a unified picture where internal shocks (and/or external Compton at the base of the jet) can provide most of the variable, high photon energy luminosity, and where the region of greatest radio emissivity is located at the head of the jet.

Hot radio spots are naturally interpreted as the working surface at the end of a jet. The jet is decelerated at a strong collisionless shock where particle acceleration and field amplification can occur. The relativistic electrons and magnetic field pressure are balanced by the ram pressure of the ambient medium. Because the source moves relativistically, aberration of light must be accounted for when calculating the observed radio light curve as well as the local direction of polarization. And as the radio hot spot is unlikely to be resolved, we can only measure the average polarization over the whole image. As a result, the breaking of symmetry of the emitting region around our line of sight is required in order to produce a net polarization. Statistical studies over a sample of tidal disruption jets, or time resolved polarimetry of different emission episodes within a single event, may teach us about the dominant emission mechanism, the

jet structure, or the magnetic field configuration within the hotspot.

It is obvious from the discussions in this paper that the dynamics of tidal disruption jets are complex, especially because of rich interactions between the jet and the surrounding medium. Confirmation was provided of the important notion that the visibility of jets, in particular the emission emanating from the head of the jet, is determined largely by the luminosity and velocity injection history of the transient jet as well as the properties of the surrounding medium. Axisymmetric hydrodynamical calculations of these jets show that the resulting dynamics are different from those predicted by one-dimensional models; interaction with the surrounding medium can not only enhance collimation but also mediate the communication delay between the base and the head of the jet. Even in the simplest case of a jet whose thrust directly scales with \dot{M}_h , complex behavior with multiple possible transitions in the observable part of the radio afterglow lifetime may be seen. The eventual resulting afterglow light curve depends fairly strongly on the properties of \dot{M}_h , especially the impact parameter β and mass of the star and the black hole. There is a good and bad side to this. On the negative side, it implies that one can not be too specific about the times at which we expect to see transitions in the observed emission. On the positive side, if and when we do see these transitions, they can be fairly constraining on the properties of the system.

5.2. *On the Nature of Swift 1644+57/GRB 110328A*

The X-ray and radio flux from the Swift 1644+57/GRB 110328 event has been interpreted as being emitted by the jet produced from the super-Eddington accretion of material resulting from the disruption of a star by a supermassive black hole. For the first ~ 30 days since the flare triggered the BAT instrument, the object exhibited tremendous variability on $\lesssim 10^4$ s timescales, with isotropic equivalent flare luminosities $> 10^{48}$ ergs/s in the soft X-rays alone. Beyond this first month of violent activity, the degree of variability decreased, and appeared to follow the predicted $t^{-5/3}$ power law associated with the late-time evolution of the fallback (Berger et al. 2012).

The initial month-long light curve plateau, punctuated by periods of extreme variability, has been presumed to be associated with the phase of the event in which the accretion rate exceeds the Eddington limit (Berger et al. 2012; Metzger et al. 2012). However, as the Eddington limit is ~ 100 times smaller than the peak accretion rate for a complete disruption by a $10^6 M_\odot$ black hole, only a disruption by a more massive black hole or a partial disruption, for which the peak accretion rates are comparable to the Eddington rate, are capable of producing such a short period of super-Eddington accretion (Figures 2 and 3). But while a partial disruption or a disruption by a heavier black hole can yield a plateau of the appropriate duration, these events peak at a much later time relative to the time of disruption, resulting in a decay slope that yields a poor match to the observed X-ray light curve.

A proposed solution to this problem is to allow the star to penetrate more deeply at pericenter (Cannizzo et

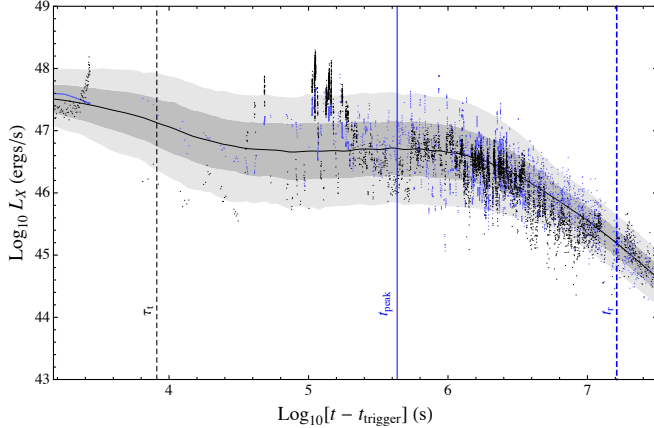


FIG. 14.— Luminosity in X-rays L_X from 2 - 10 keV for Swift J1644+57. The black points show the measured flux from the event, whereas the blue points show the realization from our stochastic model of jet emission from 10^3 realizations of a flare generated by the disruption of a $1M_\odot$ star by a 10^6M_\odot black hole that bears the most resemblance (i.e., the minimum χ^2) to the observed light curve. The sample times for the chosen realization are selected to be equal to the observation times of the Swift event. The gray contours show the 1- and 2- σ variances from the mean luminosity L_j , which is shown as the solid black curve. The black dashed vertical line shows τ_t , the orbital period at the tidal radius, the characteristic timescale of variation in our model. The blue vertical lines show timescales associated with the presented realization, with the thin line showing t_{peak} , whereas the thick line shows t_r as calculated by equation (13).

al. 2011), for which analytical approximations in which the binding energy distribution across the star is presumed to be “frozen in” at pericenter (Evans & Kochanek 1989; Lodato et al. 2009) can produce shorter flare times. These shorter flares could reproduce both the month-long plateau and the observed decay rate. However, numerical simulations by Guillochon & Ramirez-Ruiz (2012) have shown that an increase of β beyond the value for which the star is completely destroyed do not result in faster transients, with the time of peak actually tending to slightly *larger* values with increasing β for complete disruptions. For very deep encounters in which general relativistic effects are important, Laguna et al. (1993) show that while t_{peak} tends to smaller values, it does not scale as sharply as predicted by the energy freezing model, and the time at which a $\beta = 5$ and a $\beta = 10$ encounter cross the Eddington limit is almost identical. Therefore, a deep encounter is incapable of reproducing the duration of the two phases exhibited by the X-ray light curve.

We suggest an alternative model in which the flare is a standard full disruption of a main sequence star, but that the triggering of the BAT instrument and the month-long plateau are actually artifacts of variability driven at a timescale comparable to the orbital period at the tidal radius, $\tau_t = 2\pi\sqrt{r_t/GM_h}$. In this model, \dot{M}_h exceeds Eddington even during the observed $t^{-5/3}$ decay phase. Variability on this timescale could be driven by the interaction of the material that returns to pericenter with previously accreted material within the accretion disk. Hydrodynamical studies of the fallback stream have shown that the material that returns to pericenter after a disruption passes through a small nozzle region where it is compressed violently (Rosswog et al. 2009; Ramirez-Ruiz & Rosswog 2009), resulting in a rapid heating of material

that may affect the nozzle dynamics or the dynamics of the accretion disk. As both the production of the jet and the seed photons emitted by the disk are dependent on the instantaneous value of \dot{M}_h , the variability introduced by the fallback can have non-linear feedback effects which may be able to produce the observed variations in flux, as is often seen in three-dimensional magnetohydrodynamical simulations of thick accretion disks (e.g. Hawley 2009).

To model this variability, we use the method of Kelly et al. (2011), in which the stochastic luminosity variation is modeled as a single Ornstein-Uhlenbeck process with characteristic frequency $\omega = 2\pi/\tau_t$, which is then added to the mean luminosity $L_j \propto \dot{M}_h$. To match the basic character of the observed light curve, we adjust the amplitude of the driving noise depending on the degree to which L_j exceeds the Eddington ratio, with a minimum noise amplitude chosen to match the observed variability at late times. At late times, the driving noise we have selected is within a factor of a few of what is measured for steady-state AGN.

Figure 14 shows the results of this simple model in comparison to the Swift event for 10^3 random realizations of a flare generated by the disruption of a $1M_\odot$ star by a 10^6M_\odot black hole, along with the realization that happens to give the best overall fit. The observed power, assumed to follow $\dot{M}_h(t)$, is amplified by two powers of the Doppler factor, δ , with $\delta^2 = 20$ and with 10% of the luminosity assumed to be emitted in the 2 - 10 keV energy range. For each realization, the triggering time is set when the isotropic equivalent luminosity of $10^{47.5}$ erg/s is surpassed. In general, this occurs close to the peak luminosity for the choice of parameters we have selected, with the trigger itself being caused by the apex of one of the mini-flares associated with our variable component. This leads to an envelope shape that shows a subtle decline from the initial triggering event within a few τ_t , and then flattens out over tens of days until $t > a \text{ few times } t_{\text{peak}}$. If the light curve near t_{peak} is characterized by a large degree of variability, as our models predicts, the triggering event occurs either before or after t_{peak} with almost equal probability, and thus identifying the actual time of peak within the light curve itself would be difficult, if not impossible.

As argued in Section 4.4, even for the simplest assumption of $L_j \propto \dot{M}_h$, we found that the resulting structure and dynamics of the radio hot spots are very different from those predicted by the standard spherical solutions (Bloom et al. 2011; Metzger et al. 2012; Berger et al. 2012). This is mainly because at early stages when $t \leq t_{\text{peak}}$ the jet evolution is governed both by the advance of the head and by the cocoon’s pressure-driven sideways expansion into the ambient medium. The rapid decrease in luminosity at t_{peak} would be preceded by the collapse of the jet channel. The collapse of both the channel and the cocoon would proceed from the galactic nuclei outward. A model in which the hot spots are simply turned off is incompatible with hydrodynamical collapse of the source. The fact that information about the rapid decrease in luminosity at $t \gtrsim t_{\text{peak}}$ is communicated to the jet head at $t_r \gg t_{\text{peak}}$ (Figure 14) provides an attractive explanation (without the need of late time energy ejection) for the delay between the jet power x-

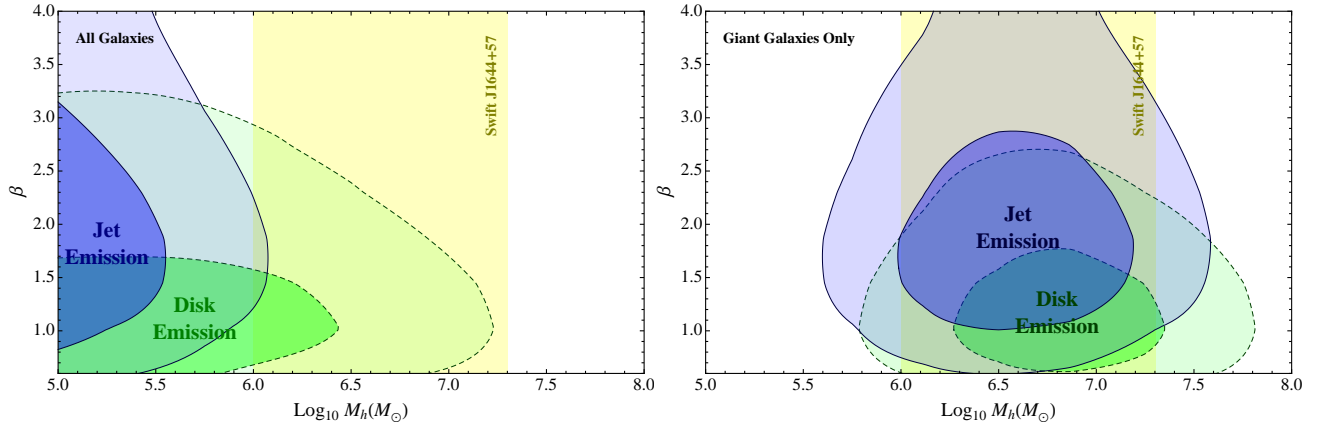


FIG. 15.— Fraction of photons received from the disk and jet emission associated with the tidal disruption of a $1 M_{\odot}$ stars as a function of the black hole mass M_h and impact parameter β . The green and blue regions show the likelihood contours for the disk and jet respectively, with the dark and light contours corresponding to 50% and 90% of all photons received. The disk contribution is calculated as in [Strubbe & Quataert \(2009\)](#), whereas the jet emission is assumed to scale as $\epsilon c^2 (\dot{M} - \dot{M}_{\text{Edd}})$. The left panel shows the probability contours considering the contribution of black holes residing in both giant and dwarf galaxies, as characterized by [Trentham and Tully 2002](#), assuming a black hole mass to bulge relation of $M_h = 10^{-2.91} M_{\text{bulge}}$ ([Merritt & Ferrarese 2001](#)). The right panel shows the probability contours for giant galaxies only. As $\dot{M} \propto M_h^{-1/2}$ and smaller black holes can foster deeper encounters where $r_p \ll r_t$, a large majority of jet-produced photons are emitted by disruptions occurring around black holes of mass $10^7 M_{\odot}$ or less, even when the contribution from dwarf galaxies is completely excluded. The limits on M_h for the black hole thought to be responsible for Swift J1644+57 are indicated by the yellow region ([Burrows et al. 2011](#)).

ray luminosity and the radio afterglow (thought to be produced by the synchrotron emitting electrons at the jet's head) seen in the Swift 1644+57/GRB 110328A event ([Berger et al. 2012](#)). The most difficult task at present is to predict t_r , the time at which the intensity of the radiation from the radio-emitting electrons which have recently emerged from the hot spot starts to rapidly decrease, which corresponds to a time $\approx r_r / (c\beta_h \Gamma_h^2)$ as measured by an observer along the line of sight. This is mainly because the hydrodynamical collapse of the channel depends sensitively on the initial Lorentz factor and opening angle of the jet as well as on the poorly known state of the surrounding environment, from the initial density gradient created by stellar wind injection to the large-scale ambient structures transversed by the jet's head at $r \gtrsim r_r$.

5.3. Rates, Lifetimes and BH Demographics

The rate of transient events coming as the result of the tidal disruption of a main sequence star is highly dependent on the population of black holes and their immediate environments. The steady-state rate of stars entering the loss cone has been estimated by many authors ([Bahcall & Wolf 1976](#); [Lightman & Shapiro 1977](#); [Shapiro 1977](#); [Syer & Ulmer 1999](#); [Wang & Merritt 2004](#)), but these calculated rates ignore mass segregation, the mass function of stars within the sphere of influence ([Bahcall & Wolf 1977](#)), the importance of black hole mergers ([Chen et al. 2009](#); [Stone & Loeb 2011](#)), and interactions between the central cluster and the host galaxy ([Magorrian & Tremaine 1999](#); [Merritt 2009](#)), all of which may affect the rate of stellar disruption. As implied by the number of AGN flares thought to result from tidal disruptions ([Gezari et al. 2009](#)), the average rate of disruption is known to be $\sim 10^{-5}$ events $\text{yr}^{-1} \text{gal}^{-1}$, but how these events are distributed among galaxies remains an open question. Given these uncertainties, we assume that the rate of disruption is not dependent on either black hole or galaxy properties for the remainder of this section.

Jets are thought to form in optically thick accretion flows resulting from accretion rates that are in excess of Eddington ([Quataert 2001](#); [Narayan & McClintock 2008](#)). The mass function of stars around black holes may be substantially different than the standard Kroupa IMF function ([Kroupa 2001](#)), but the average stellar mass is on the order of $1 M_{\odot}$ for all black holes. As a result, the peak accretion rate simply scales with the orbital period at the tidal radius, which low-mass black holes can more easily produce jets from the disruption of a star given their smaller Eddington limits. This biases the production of jets to low-mass black holes, of which our census is growing ([Ramya et al. 2011](#); [Xiao et al. 2011](#)) but is still too small to definitively relate to galactic velocity dispersion as has been demonstrated convincingly with black holes of $M_h \gtrsim 10^6 M_{\odot}$ ([Merritt & Ferrarese 2001](#); [Gültekin et al. 2009](#); [Beifiori et al. 2011](#)). Emission resulting from disks, on the other hand, is thought to extend well below the Eddington rate, and thus the only requirement to produce a transient disk from the disruption of a star is that the pericenter of the orbit does not lie within the black hole's Schwarzschild radius. As a result, disks are not likely to be produced by disruptions for black holes of mass $\gtrsim 10^8 M_{\odot}$.

Figure 15 shows the fraction of the total bolometric flux received by an observer from both the jet and disk components resulting from the tidal disruptions of a $1 M_{\odot}$ stars. The majority of stars that are fed into the black hole originate near the black hole's sphere of influence from the *pinhole* regime of disruption ([Lightman & Shapiro 1977](#)), and thus the differential contribution of stars as a function of the impact parameter β approximately scales as β^{-2} . The left panel shows the expected contribution of events to each emission type assuming that black holes of all masses are equally common, an assumption which is not unreasonable given the potentially flat black hole mass function at low black hole mass as measured by [Greene & Ho \(2007\)](#). If the trend of $M_h - \sigma$ continued to lower black hole masses, this plot would

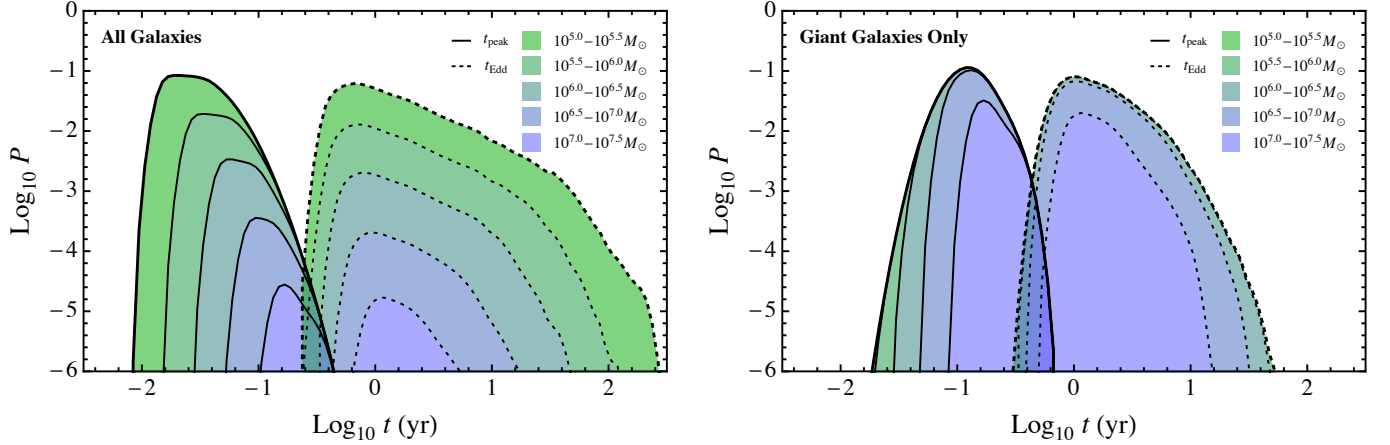


FIG. 16.— Stacked probability histograms showing contribution to measured peak times t_{peak} and time at which the accretion rate falls below the Eddington limit t_{Edd} . Each colored region corresponds to a range of black hole masses as annotated in the upper right of each panel, with the solid lines corresponding to t_{peak} and the dashed lines corresponding to t_{Edd} . The left and right panels show the same two galaxy distributions as described in the caption for Figure 15.

be further biased to black holes of lower mass given the large population of low-mass galaxies. If the trend does not continue and black holes of $\lesssim 10^6 M_\odot$ are rare, both emission components are biased to black holes of larger mass, as shown in the right panel of Figure 15. The limits on the mass of the black hole associated with the transient event Swift J1644+57 coming from the variability timescale and the $M_{\text{h}} - \sigma$ relation (Bloom et al. 2011; Burrows et al. 2011) agree quite well with a black hole mass function that excludes low-mass black holes, but given the associated uncertainties in the mass determination even a completely flat distribution of black hole masses cannot be completely ruled out.

An additional constraint on the progenitors of events similar to Swift J1644+57 is the time at which \dot{M}_{h} reaches its peak value, t_{peak} , and the time at which \dot{M}_{h} drops below \dot{M}_{Edd} , t_{Edd} . Under the same assumptions used to generate Figure 15, we show in Figure 16 the probability P of observing a flare with a given value of t_{peak} and t_{Edd} . We find that the most probable t_{peak} is a few to tens of days, whereas the most probable $t_{\text{Edd}} \sim 1 - 10$ years, depending on whether or not low mass central black holes are common. Both distributions are consistent with the Swift event, which our model suggests was caught within days of the peak, and remained above the Eddington limit for ~ 1 year.

The discovery of flaring black hole candidates in nearby

galaxies by Swift will continue to elucidate the demography of the quasar and AGN population, while also enabling us to distinguish between various theoretical models of tidal disruption. As the feeding rate evolves dramatically over only a period of weeks to months, the powering of these formerly dead quasars offers a unique perspective into how the production of jets from black holes depends on the rate at which they are fed and the state of the environment in which they reside. These events can provide valuable insight into the physical mechanisms that operate near massive black holes that are not continually active, a prospect that is otherwise only possible through the study of the nearest few massive black holes. As the number of events increases, the range of possible models that can simultaneously explain the luminosity, variability, color, and time-evolution of these events will diminish, enabling a firm characterization of one of the dominant feeding mechanisms of massive black holes in the local universe.

We have benefited from many useful discussions with E. Berger, J. Bloom, D. Giannos, J. Grindlay, D. Kasen, B. Kelly, W. Lee, B. Metzger, S. Piran, A. Socrates, A. Soderberg, J. Trump, and A. Zauderer. This research was supported by the David and Lucille Packard Foundation (ERR, JG and FDC), the NASA Earth and Space Science Fellowship (JG), and the NSF (ERR and JN) (AST- 0847563).

REFERENCES

- Aliu, E., Arlen, T., Aune, T., et al. 2011, *ApJ*, 738, L30
- Ayal, S., & Piran, T. 2001, *ApJ*, 555, 23
- Bahcall, J. N., & Wolf, R. A. 1977, *ApJ*, 216, 883
- Bahcall, J. N., & Wolf, R. A. 1976, *ApJ*, 209, 214
- Barai, P., Proga, D., & Nagamine, K. 2011, arXiv:1112.5483
- Begelman, M. C., Blandford, R. D., & Rees, M. J. 1984, *Reviews of Modern Physics*, 56, 255
- Begelman, M. C., & Cioffi, D. F. 1989, *ApJ*, 345, L21
- Beifiori, A., Courteau, S., Corsini, E. M., & Zhu, Y. 2011, *MNRAS*, 1886
- Berger, E., Zauderer, A., Pooley, G. G., et al. 2012, *ApJ*, 748, 36
- Blandford, R. D., & McKee, C. F. 1976, *Physics of Fluids*, 19, 1130
- Bloom, J. S., Giannos, D., Metzger, B. D., et al. 2011, *Science*, 333, 203
- Bromberg, O., Nakar, E., Piran, T., & Sari, R. 2011, *ApJ*, 740, 100
- Burrows, D. N., Kennea, J. A., Ghisellini, G., et al. 2011, *Nature*, 476, 421
- Campana, S., Lodato, G., D’Avanzo, P., et al. 2011, *Nature*, 480, 69
- Cannizzo, J. K., Troja, E., & Lodato, G. 2011, *ApJ*, 742, 32
- Cenko, S. B., Krimm, H. A., Horesh, A., et al. 2011, arXiv:1107.5307
- Chen, X., Madau, P., Sesana, A., & Liu, F. K. 2009, *ApJ*, 697, L149
- De Colle, F., Granot, J., López-Cámara, D., & Ramirez-Ruiz, E. 2012a, *ApJ*, 746, 122
- De Colle, F., Ramirez-Ruiz, E., Granot, J., & Lopez-Camara, D. 2012b, arXiv:1111.6667

- Evans, C. R., & Kochanek, C. S. 1989, *ApJ*, 346, L13
- Fender, R., Corbel, S., Tzioumis, T., et al. 1999, *ApJ*, 519, L165
- Frank, J., & Rees, M. J. 1976, *MNRAS*, 176, 633
- Fryxell, B., et al. 2000, *ApJS*, 131, 273
- Garcia, M. R., Hextall, R., Baganoff, F. K., et al. 2010, *ApJ*, 710, 755
- Gehrels, N., Ramirez-Ruiz, E., & Fox, D. B. 2009, *ARA&A*, 47, 567
- Gezari, S., Heckman, T., Cenko, S. B., et al. 2009, *ApJ*, 698, 1367
- Giannios, D., & Metzger, B. D. 2011, *MNRAS*, 416, 2102
- Greene, J. E., & Ho, L. C. 2007, *ApJ*, 667, 131
- Guillochon, J., Ramirez-Ruiz, E., Rosswog, S., & Kasen, D. 2009, *ApJ*, 705, 844
- Guillochon, J., Ramirez-Ruiz, E., & Lin, D. 2011, *ApJ*, 732, 74
- Guillochon, J., & Ramirez-Ruiz, E. 2012, In Preparation
- Gültekin, K., Richstone, D. O., Gebhardt, K., et al. 2009, *ApJ*, 698, 198
- Hawley, J. F. 2009, *Ap&SS*, 320, 107
- Holzer, T. E., & Axford, W. I. 1970, *ARA&A*, 8, 31
- Kelly, B. C., Sobolewska, M., & Siemiginowska, A. 2011, *ApJ*, 730, 52
- Kobayashi, S., Piran, T., & Sari, R. 1997, *ApJ*, 490, 92
- Krautter, A., Henriksen, R. N., & Lake, K. 1983, *ApJ*, 269, 81
- Krolik, J. H., & Piran, T. 2011, *ApJ*, 743, 134
- Krolik, J. H., & Piran, T. 2012, *ApJ*, 749, 92
- Kroupa, P. 2001, *MNRAS*, 322, 231
- Laguna, P., Miller, W. A., Zurek, W. H., & Davies, M. B. 1993, *ApJ*, 410, L83
- Lazzati, D., Morsony, B. J., Blackwell, C. H., & Begelman, M. C. 2011, *arXiv:1111.0970*
- Levan, A. J., Tanvir, N. R., Cenko, S. B., et al. 2011, *Science*, 333, 199
- Lightman, A. P., & Shapiro, S. L. 1977, *ApJ*, 211, 244
- Lodato, G., King, A. R., & Pringle, J. E. 2009, *MNRAS*, 392, 332
- Loeb, A., & Ulmer, A. 1997, *ApJ*, 489, 573
- Naiman, J. P., Ramirez-Ruiz, E., & Lin, D. N. C. 2012, submitted to *ApJ*
- Magorrian, J., & Tremaine, S. 1999, *MNRAS*, 309, 447
- Matzner C. D., 2003, *MNRAS*, 345, 575
- Meier, D. L., Koide, S., & Uchida, Y. 2001, *Science*, 291, 84
- Merritt, D. 2009, *ApJ*, 694, 959
- Merritt, D., & Ferrarese, L. 2001, *ApJ*, 547, 140
- Metzger, B. D., Giannios, D., & Mimica, P. 2012, *MNRAS*, 420, 3528
- Müller, J. M., Gültekin, K. 2011, *ApJ*, 738, L13
- Mirabel, I. F., & Rodríguez, L. F. 1999, *ARA&A*, 37, 409
- Najarro, F., Krabbe, A., Genzel, R., et al. 1997, *A&A*, 325, 700
- Narayan, R., & McClintock, J. E. 2008, *newAR*, 51, 733
- Ouyed, R., Staff, J., & Jaikumar, P. 2011, *ApJ*, 743, 116
- Quataert, E. 2001, Probing the Physics of Active Galactic Nuclei, 224, 71
- Quataert, E. 2004, *ApJ*, 613, 322
- Quataert, E., & Kasen, D. 2011, *MNRAS*, L360
- Ramirez-Ruiz, E., Celotti, A., & Rees, M. J. 2002, *MNRAS*, 337, 1349
- Ramirez-Ruiz, E., & Lloyd-Ronning, N. M. 2002, *New Astronomy*, 7, 197
- Ramirez-Ruiz, E., & MacFadyen, A. I. 2010, *ApJ*, 716, 1028
- Ramirez-Ruiz, E., & Rosswog, S. 2009, *ApJ*, 697, L77
- Ramya, S., Prabhu, T. P., & Das, M. 2011, *MNRAS*, 418, 789
- Rees, M. J. 1988, *Nature*, 333, 523
- Rees, M. J., & Meszaros, P. 1994, *ApJ*, 430, L93
- Rosswog, S., Ramirez-Ruiz, E., & Hix, W. R. 2009, *ApJ*, 695, 404
- Shao, L., Zhang, F.-W., Fan, Y.-Z., & Wei, D.-M. 2011, *ApJ*, 734, L33
- Shapiro, S. L. 1977, *ApJ*, 217, 281
- Socrates, A. 2011, *arXiv:1105.2557*
- Stone, N., & Loeb, A. 2011, *MNRAS*, 412, 75
- Strubbe, L. E., & Quataert, E. 2009, *MNRAS*, 400, 2070
- Syer, D., & Ulmer, A. 1999, *MNRAS*, 306, 35
- Taub, A. H. 1948, *Physical Review*, 74, 328
- Tout, C. A., Pols, O. R., Eggleton, P. P., & Han, Z. 1996, *MNRAS*, 281, 257
- Trentham, N., & Tully, R. B. 2002, *MNRAS*, 335, 712
- van Velzen, S., KÖrding, E., & Falcke, H. 2011, *MNRAS*, 417, L51
- Wang, J., & Merritt, D. 2004, *ApJ*, 600, 149
- Wiersema, K., van der Horst, A. J., Levan, A. J., et al. 2011, *arXiv:1112.3042*
- Woosley, S. E., & Heger, A. 2011, *arXiv:1110.3842*
- Xiao, T., Barth, A. J., Greene, J. E., et al. 2011, *ApJ*, 739, 28
- Zauderer, B. A., Berger, E., Soderberg, A. M., et al. 2011, *Nature*, 476, 425